

Neural markers of suppression in impaired binocular vision

Freya A. Lygo^{1,2}, Bruno Richard³, Alex R. Wade^{1,4}, Antony B. Morland^{1,4} & Daniel H. Baker^{1,4,5}

1. Department of Psychology, University of York, Heslington, York, UK

2. Institute of Cognitive Neuroscience, University College London, London, UK

3. Department of Mathematics and Computer Science, Rutgers University–Newark, Newark, New Jersey, USA

4. York Biomedical Research Institute, University of York, Heslington, York, UK

5. Corresponding author: daniel.baker@york.ac.uk

Precis (35 words)

Evidence of atypical interocular suppression in individuals with impaired binocular vision was obtained using EEG and fMRI, with a single experimental paradigm. This may underlie the deficits in stereopsis experienced by treated amblyopes.

Keywords: interocular suppression; dichoptic; fMRI; SSVEP; V1

Financial support: This work was supported in part by a Wellcome Trust (ref: 105624) grant, through the Centre for Chronic Diseases and Disorders (C2D2) at the University of York. FL was funded by a PhD student from the University of York. The sponsor or funding organization had no role in the design or conduct of this research.

Conflict of interest: No conflicting relationship exists for any author

Running head: Suppression in impaired binocular vision

This article contains additional online-only material. The following should appear online-only: Figure S1, Figure S2.

33 **Abstract**

34
35 Objective/Purpose: Even after conventional patching treatment, individuals with a history of
36 amblyopia typically lack good stereo vision. This is often attributed to atypical suppression
37 between the eyes, yet the specific mechanism is still unclear. Guided by computational models of
38 binocular vision, we tested explicit predictions about how neural responses to contrast might differ
39 in individuals with impaired binocular vision.

40
41 Design: A 5×5 factorial repeated measures design was used, in which all participants completed
42 a set of 25 conditions (stimuli of different contrasts shown to the left and right eyes).

43
44 Participants: 25 individuals with a history of amblyopia, and 19 control participants with typical
45 visual development, participated in the study.

46
47 Methods: Neural responses to different combinations of contrast in the left and right eyes, were
48 measured using both electroencephalography (EEG) and functional magnetic resonance imaging
49 (fMRI). Stimuli were sinusoidal gratings with a spatial frequency of 3c/deg, flickering at 4Hz. In
50 the fMRI experiment, we also ran population receptive field and retinotopic mapping sequences,
51 and a phase-encoded localiser stimulus, to identify voxels in primary visual cortex (V1) sensitive
52 to the main stimulus.

53
54 Main outcome measures: The main outcome measures were the signal-to-noise ratio of the
55 steady state visual evoked potential, and the fMRI β weights from a general linear model.

56
57 Results: Neural responses generally increased monotonically with stimulus contrast. When
58 measured with EEG, responses were attenuated in the weaker eye, consistent with a fixed tonic
59 suppression of that eye. When measured with fMRI, a low contrast stimulus in the weaker eye
60 substantially reduced the response to a high contrast stimulus in the stronger eye. This effect was
61 stronger than when the stimulus-eye pairings were reversed, consistent with unbalanced dynamic
62 suppression between the eyes.

63
64 Conclusions: Measuring neural responses using different methods leads to different conclusions
65 about visual differences in individuals with impaired binocular vision. Both of the atypical
66 suppression effects may relate to binocular perceptual deficits, e.g. in stereopsis, and we
67 anticipate that these measures could be informative for monitoring the progress of treatments
68 aimed at recovering binocular vision.

69

70 **Introduction**

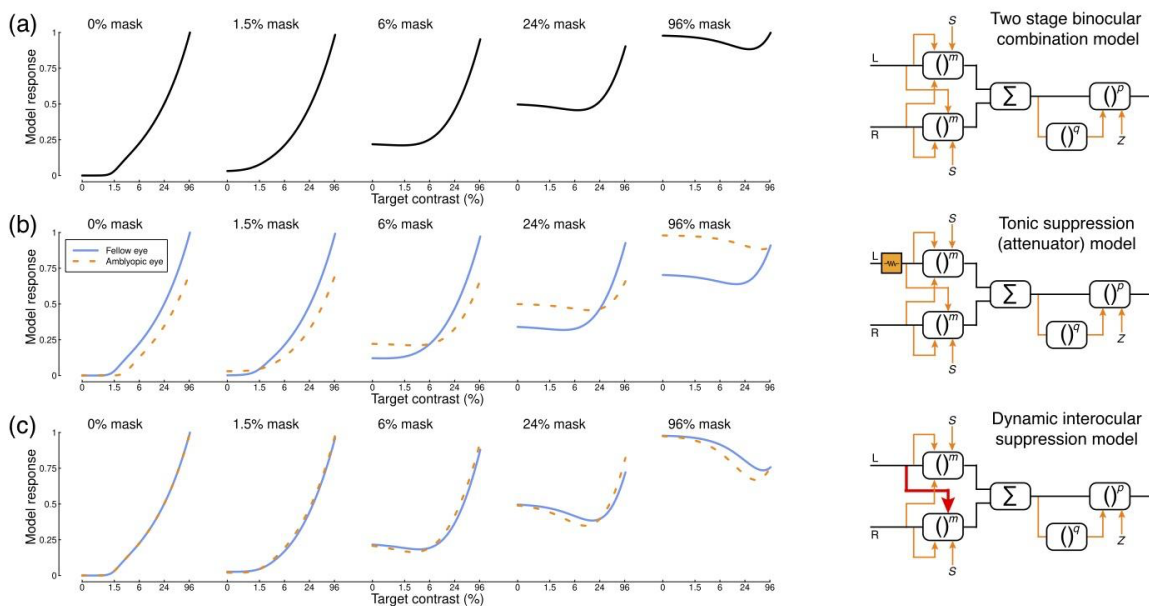
71
72 The binocular visual system is exquisitely sensitive, and has the ability to detect differences
73 (disparities) between the eyes of well below one minute of arc¹. This results in a vivid perception
74 of depth from stereopsis² that benefits everyday tasks such as fine motor control (e.g. threading
75 a needle) and the judgement of relative object distance (e.g. during driving). But in a substantial
76 minority of individuals (around 1.4%³), an optical (e.g. anisometropia) or muscular (e.g.
77 strabismus) asymmetry between the eyes during childhood disrupts the development of binocular
78 vision. This can lead to amblyopia, in which vision through the affected eye is significantly
79 impaired⁴. Such problems can be treated to some extent by orthoptic or surgical interventions,
80 which recover sensitivity in the weaker eye in a proportion of cases⁵. But even if treatment is
81 successful in improving vision in the amblyopic eye, binocular vision may not be restored and
82 stereopsis rarely reaches normal levels⁶. An enduring mystery is the identity of the neural
83 mechanism that disrupts binocular vision, even in situations where the eyes have similar acuity
84 and sensitivity.

85
86 In clinical practice, binocular visual disturbances in amblyopia are typically attributed to a process
87 of suppression, whereby the fellow eye suppresses signals from the amblyopic eye^{7,8,9}. This
88 suppression could take several different forms. For example, 'tonic' suppression should persist
89 even when there is no input to the fellow eye (e.g. if it is closed, patched or pressure blinded, or
90 simply shown a blank display). This amounts to a fixed attenuation of the signal in the amblyopic
91 eye that is invariant to signals from the fellow eye¹⁰. Alternatively, a more 'dynamic' form of
92 suppression would depend on the current stimulation of the two eyes, such that higher contrasts
93 in one eye produce greater suppression of the other eye. Interocular suppression has been widely
94 studied in intact binocular vision, and has several perceptual consequences, such as ocularity
95 invariance (the observation that our general perception of the world is unchanged whether one or
96 both eyes are open¹¹) and binocular rivalry (the alternation in perception between conflicting
97 images shown to the two eyes¹²). Impaired binocular vision might result from an imbalance of
98 these existing processes of interocular suppression.

99
100 Distinguishing between these, and other, explanations for binocular impairments has proved
101 challenging. In some psychophysical paradigms, such as dichoptic contrast discrimination, similar
102 performance can result even over a wide range of relative amounts of suppression between the
103 eyes¹⁰. In other paradigms, tonic and dynamic suppression are equally able to account for the
104 results¹³. Isolating a direct neural measure of suppression would allow us to distinguish between
105 different models, and potentially provide an objective index of binocular impairment that could be
106 used to track improvements during treatment. In the present study we measured visual responses
107 to stimuli of different contrasts directly with two methods: functional magnetic resonance imaging
108 (fMRI) and electroencephalography (EEG). These methods have complementary strengths and
109 weaknesses: fMRI has excellent spatial precision, but poor temporal resolution, whereas EEG
110 has poor spatial precision, but good temporal resolution. Previous work measuring visual
111 responses in amblyopia with one or other of these methods has reported generally weaker
112 responses to stimuli in the amblyopic eye^{14,15}. However, the two techniques have not previously
113 been directly compared using common stimuli.

114
 115
 116
 117
 118
 119
 120
 121
 122
 123
 124
 125
 126
 127
 128
 129
 130

Here we use both methods to measure contrast-response functions (Figure 1a) for factorial combinations of contrast shown to the left and right eyes (Figure 2g; see also¹¹). We plot the results as a series of functions, where stimuli of increasing contrast are shown to one eye (the ‘target’ stimuli) in the presence of a fixed-contrast (but otherwise identical) stimulus in the other eye (the ‘mask’ stimulus). The general character of these functions can be predicted by contemporary models of binocular signal combination^{16,17}, and correspond well to previous measurements in intact binocular visual systems using both fMRI¹⁷ and EEG¹⁸. When the mask is absent (0% contrast), the model produces a monotonically increasing monocular contrast response function (left-most curve in Figure 1a). As mask contrast increases, the overall response becomes larger because it combines the target and mask signals together. However, interocular suppression causes a surprising reduction in the response to a high contrast mask when a target of intermediate contrast is added^{11,19}. This produces the u-shaped function shown in the final curve of Figure 1a - the response increase caused by excitation is outweighed by the response reduction caused by suppression. Responses therefore go down before they go up, giving a direct measure of interocular suppression.



131
 132
 133
 134
 135
 136
 137
 138
 139
 140
 141
 142

Figure 1: Model predictions and diagrams. Panel (a) shows predictions of the two-stage model (Meese et al., 2006) for different combinations of mask and target contrasts shown to the left and right eyes. The model diagram features multiple stages of gain control (boxes), exponentiation (to powers m , p and q), inhibition (orange arrows), and binocular summation (denoted by Σ). Panel (b) shows a variant of the same model¹⁰, where the input to the left eye is attenuated prior to any other processing (orange box in the diagram). This affects the model’s behaviour by reducing the response to the affected (e.g. amblyopic) eye (orange dashed curves). Panel (c) shows a further variant in which there is stronger inhibition from one eye onto the other (red arrow in the diagram). This has no effect for monocular stimulation (leftmost function), but increases suppression with high mask contrasts (rightmost functions). Further model details and equations are given in Appendix 1.

143 We can disrupt the model shown in Figure 1a in two key ways. First, we can implement tonic
144 suppression by attenuating the signal in one eye by a constant factor¹⁰. This reduces the response
145 in the affected eye, and also weakens its impact on the fellow eye (Figure 1b). Second, we can
146 implement dynamic suppression by increasing the weight of suppression from one eye onto the
147 other (Figure 1c). This has no effect on monocular presentations (as there is no signal in the
148 opposite eye to cause suppression), but with high-contrast masks there is a much greater
149 reduction in response for intermediate signal contrasts (the u-shaped functions in the right-most
150 plot become deeper). This experimental paradigm therefore has the potential to distinguish
151 between these two types of suppression.

152

153 Our aim in this study was to empirically test specific predictions of these competing models by
154 measuring neural responses with fMRI and EEG to a common set of visual stimuli. In addition to
155 testing control participants with typical binocular vision, we also recruited individuals with a history
156 of binocular disturbance. Although these participants do not all currently meet the diagnostic
157 criteria for amblyopia (owing to successful treatment), they would very likely have done so in
158 childhood and/or had they not been treated. Given the widespread incidence of treatment in
159 countries with developed healthcare systems, understanding the residual binocular deficits in
160 treated amblyopes is of substantial clinical importance. To summarise our results, we find
161 attenuated responses to stimuli in the amblyopic eye when measured using EEG, and increased
162 and asymmetrical interocular suppression in individuals with impaired binocular vision when
163 measured using fMRI. Surprisingly this takes the form of stronger suppression of the dominant
164 eye by the weaker eye.

165

166 **Methods**

167

168 *Participants*

169

170 A total of 44 adult participants completed the EEG experiment, 19 of whom were control
171 participants with no history of binocular visual abnormalities, and clinically normal vision. The
172 remaining 25 participants had been diagnosed with amblyopia, or treated for strabismus during
173 childhood (see Table 1 for further details). Their ages ranged from 17 to 49, with a mean age of
174 23.8 years (SD of 7.7 years). Approximately half of these participants (12/25, highlighted in bold)
175 still met the diagnostic criteria for amblyopia at the time of testing, based on a corrected visual
176 acuity difference of two lines or more between the eyes. The MRI experiments were completed
177 by 10 of the control participants, and 12 of the patients (A1 - A12 in Table 1). Participants gave
178 written informed consent, and received financial compensation for their time (£20 per experiment).
179 The study protocols were approved by the research governance committee of the York
180 Neuroimaging Centre, and were consistent with the original wording of the Declaration of Helsinki.

181

182 *Apparatus and stimuli*

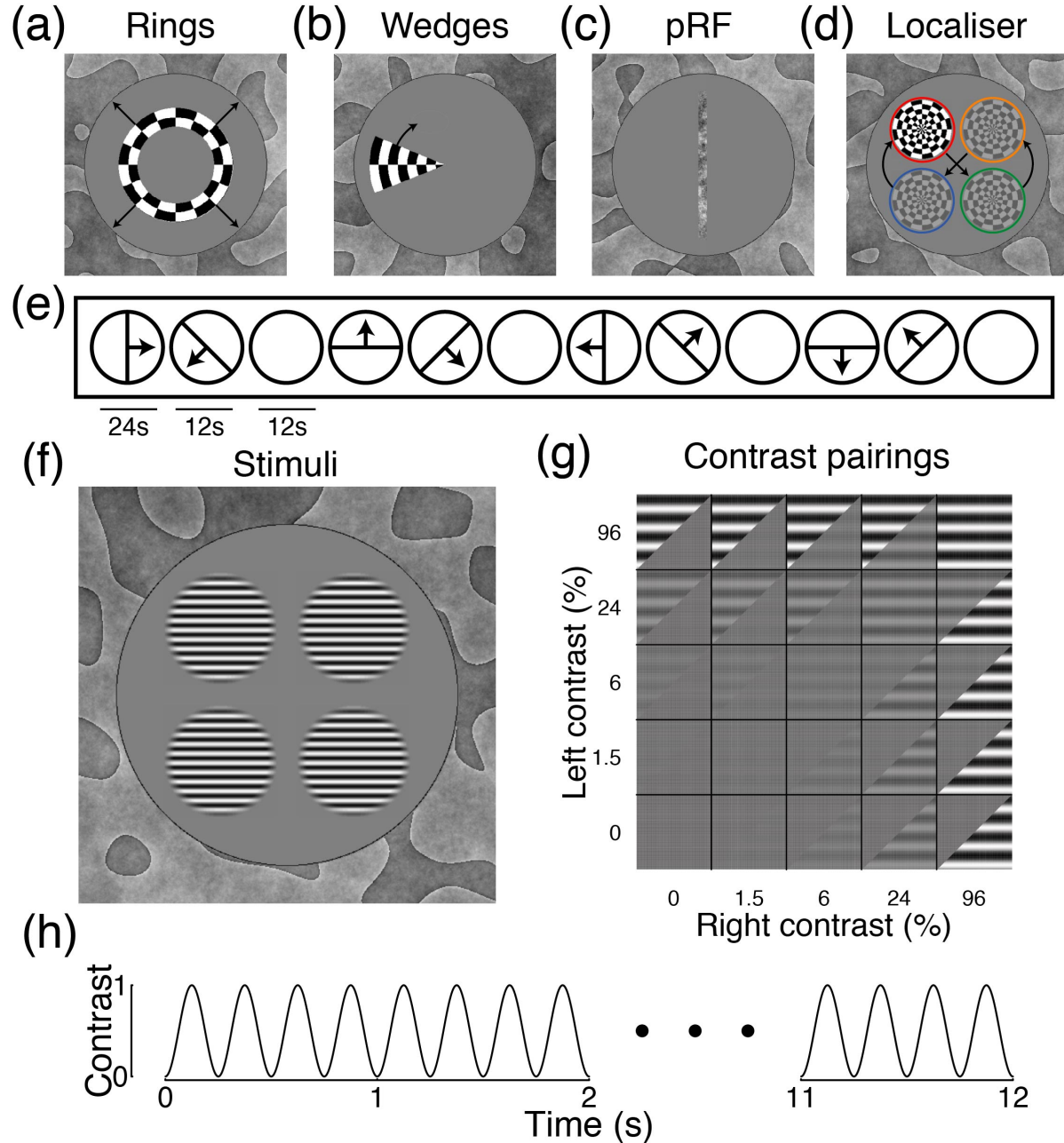
183

184 In the MRI scanner, stimuli were displayed using a ProPixx DLP projector (VPixx Ltd., Quebec,
185 Canada) with a refresh rate of 120Hz, and a resolution of 1920 × 1080 pixels. Viewed from a
186 distance of 57cm, there were 36 pixels per degree of visual angle. The projector was driven by a

187 high performance PC. A circular polariser interleaved images intended for the left and right eyes
 188 (effective refresh rate of 60Hz per eye). Images were projected onto a custom acrylic display
 189 panel that maintained the polarisation, and viewed through a front-silvered mirror and passive
 190 stereo polarizer glasses. The maximum luminance was 356cd/m² when viewed through the
 191 glasses. In the EEG lab, stimuli were displayed using a gamma-corrected ViewPixx 3D LCD
 192 display (VPixx Ltd.) with a refresh rate of 120Hz, and a resolution of 1920 × 1080 pixels. Viewed
 193 from a distance of 57cm, there were 36 pixels per degree of visual angle. The display was driven
 194 by a Mac Pro computer. Active stereo shutter goggles (NVidia 3D Vision), synchronised by an
 195 infrared signal, allowed segregation of images to the left and right eyes. Through the goggles, the
 196 maximum luminance was 26cd/m². Both display systems had low levels of crosstalk, as measured
 197 using a photometer²⁰. All experiments were programmed in Matlab, using the Psychophysics
 198 Toolbox extensions²¹⁻²³.

200 Table 1: summary of patient demographics, clinical history and acuity measurements. Those highlighted in
 201 bold currently meet the clinical criteria for amblyopia (acuity difference of two lines or more on a Snellen
 202 chart). None of the participants had a residual strabismus.

Participant	Sex	Amblyopic Eye	R acuity	L acuity	Stereo acuity	Detected	Patching	Surgery	Correction
A1	F	Right	20/32	20/25	None	18 mo	1 - 6 y	<18mo	None
A2	M	Right	20/50	20/20	80s	9 y	9 y	None	None
A3	M	Left	20/20	20/50	140s	4 y	4 y	None	None
A4	M	Left	20/20	20/32	140s	18 mo	5 y	18 mo	None
A5	F	Left	20/20	20/40	40s	5 y	5 - 6 y	None	LE: -2.5; RE: + 0.75
A6	M	Left	20/20	20/40	80s	4 y	4 y	None	None
A7	F	Right	20/40	20/20	60s	~10 y	None	None	None
A8	F	Left	20/40	20/80	None	11 y	11 - 12 y	None	None
A9	F	Left	20/16	20/16	400s	6 y	None	None	None
A10	F	Left	20/16	20/20	None	18 mo	4 y	None	LE: +4; RE:+3.75
A11	M	Right	20/20	20/20	140s	5 y	5 y	None	None
A12	F	Right	20/20	20/20	400s	3 y	None	3 & 4 y	None
A13	F	Left	20/20	20/50	None	5 y	5 - 6 y	None	None
A14	F	Left	20/25	20/32	40s	4 y	4 - 6 y	None	None
A15	M	Left	20/16	20/32	None	20 mo	4 y	1 & 7 y	Not known
A16	M	Right	20/120	20/25	400s	9 y	None	None	None
A17	M	Right	20/100	20/16	None	4 y	4 y	None	None
A18	F	Left	20/16	20/16	None	7 y	7 - 10 y	None	None
A19	F	Left	20/20	20/200	None	18 mo	18 mo	None	None
A20	M	Left	20/50	20/50	200s	<6 y	6 y	None	None
A21	F	Right	20/20	20/16	40s	5 y	5 y	None	LE: -1.25; RE: -1.75
A22	F	Left	20/20	20/32	None	~6 y	6 - 7 y	~6 y	LE: +10.5; RE: +9.5
A23	M	Right	20/32	20/20	400s	5 y	5 y	16 y	None
A24	F	Left	20/20	20/40	40s	4 y	4 - 5 y	None	None
A25	M	Left	20/16	20/20	140s	2 y	2 - 3 y	None	None



204
 205
 206
 207
 208
 209
 210
 211
 212
 213
 214

Figure 2: Example stimuli and methodological details. Panels (a,b,c,d,f) show stimuli used in different parts of the study. Panels (a,b) show ring and wedge plaid stimuli used in retinotopic mapping, with black arrows (not presented) indicating the direction of motion. Panel (c) shows the noise bar used in population receptive field (pRF) mapping, which followed the temporal sequence illustrated in panel (e). Panel (d) shows the plaid localiser stimulus, which followed the positional sequence indicated by the arrows (only one plaid was visible in a given 6-second window, and the coloured rings were not shown). Panel (f) shows the sine-wave grating stimuli used to measure contrast response functions. These were presented to the left and right eyes in different contrast combinations, as illustrated in panel (g). The gratings flickered on and off for 12 seconds according to a 4Hz sine-wave, as shown in panel (h).

215 Retinotopic mapping involved binocularly presented ring and wedge stimuli constructed from a
216 radial square wave plaid, as illustrated in Figure 2a,b. The plaid had an angular wavelength of 45
217 degrees (i.e. 8 complete cycles in 360 degrees), a radial frequency of 0.8 cycles per degree, and
218 flickered in counterphase at 4Hz. Expanding rings had a width of 1 plaid cycle, and a period of 12
219 seconds per sequence (4 ring positions). Rotating wedges were 45 degrees (1 cycle) wide, with
220 a period of 24 seconds per rotation (8 positions in 45 degree clockwise steps). Population
221 receptive field (pRF) mapping used a drifting bar (0.5×10 degrees) of dynamic $1/f$ noise, with an
222 RMS contrast of 0.2 (see Figure 2c). The bar drifted at a speed of 0.4 deg/sec, and followed the
223 sequence illustrated in Figure 2e. The pRF stimulus was presented to either the left or right eye
224 in different blocks, with the other eye viewing mean luminance. We used a phase-encoded
225 localiser stimulus, constructed from a radial plaid with a width of 4 degrees (see Figure 2d),
226 presented binocularly. The localiser stimulus counterphase flickered at 4Hz, and changed position
227 every 6 seconds, according to the sequence illustrated in Figure 2d. Each stimulus location had
228 an x-y offset of ± 2.34 degrees from fixation. Stimuli for the main experiments were four horizontal
229 sine-wave gratings with a spatial frequency of 3c/deg, a cosine-blurred spatial window, and a
230 width of 4 degrees (see Figure 2f). Five different Michelson contrast values (defined as $100 \cdot (L_{\max} - L_{\min}) / (L_{\max} + L_{\min})$, where L is luminance) were presented in different combinations (see Figure 2g).
231 The stimuli flickered sinusoidally between 0 and their nominal contrast (on/off flicker) at a
232 frequency of 4Hz (see Figure 2h). The grating stimuli had x-y offsets of ± 2.34 degrees from
233 fixation. In all experiments, a static binocular texture was presented to aid fusion. This was
234 constructed from low spatial frequency bandpass filtered noise, and filled the display beyond the
235 central 12 degree stimulus aperture (see Figure 2 for examples).
236

237

238 *MRI acquisition*

239

240 All MRI data were acquired using a GE 3T HDx Excite MRI scanner. We collected two high
241 resolution T1-weighted structural scans (TR 7.8 ms; TE 3 ms; voxel size $1 \times 1 \times 1$ mm; 12° flip
242 angle; matrix size 256×256 ; FOV 256 mm), and two T2*-weighted fast gradient recalled echo
243 scans (TR 400 ms; TE 4.2 ms; voxel size $1 \times 1 \times 2$ mm; 25° flip angle; matrix size 128×128 ;
244 FOV 260×260 mm), using an 8-channel surface coil (Nova Medical, Wilmington, MA, USA). We
245 acquired functional images using an EPI sequence with a 16-channel posterior surface coil (Nova
246 Medical, Wilmington, MA, USA), to optimize signal-to-noise ratio at the occipital pole. The slice
247 prescription covered the region containing the calcarine sulcus and occipital pole with 39 axial
248 slices (TR 3000 ms; TE 30 ms; voxel size $2 \times 2 \times 2$ mm; 90° flip angle; matrix size 96×96 ; FOV
249 192×192 mm). We also acquired an in-plane proton density scan using the same slice
250 prescription to aid alignment with the structural scans.

251

252 Participants completed the MRI experiments in two sessions. In the first session, we collected the
253 structural scans, and the retinotopic mapping and pRF data. Each pRF sequence lasted 396
254 seconds (132 TRs), and either the left or right eye was stimulated. Two repetitions for each eye
255 were completed. The retinotopic mapping (ring and wedge) sequences were collected as a single
256 scan lasting 204 seconds (68 TRs). In the second session, the phase-encoded localiser and
257 contrast response function data were collected. The localiser scan lasted 156 seconds (52 TRs),

258 and consisted of a blank period (12 seconds), followed by 6 repetitions of the localiser sequence.
259 The contrast response function sequence lasted 612 seconds (204 TRs), and tested each of the
260 25 conditions (see Figure 2g) once, with 12-second blank periods between each 12-second trial.
261 This was repeated four times for each participant. During all functional scans, participants
262 performed a fixation task, in which they monitored a grid of 9 squares (3x3, each 0.14 degrees
263 wide) with random luminances in the centre of the screen. They were instructed to press a button
264 whenever the fixation marker was changed by re-randomising the luminances. This occurred at
265 randomly determined times, on average once every 48 seconds (i.e. once every two trials). The
266 task was intended to maintain attention and fixation, and we did not record the responses.

267

268 *MRI analysis*

269

270 Primary MRI analysis was conducted in Matlab using the mrVista toolbox
271 (<https://github.com/vistalab/vistasoft>). Functional data were motion-corrected within and between
272 scans, and aligned to the in-plane (proton density) scan, and subsequently to the participant's
273 anatomical space. The first 12 seconds (4 TRs) of each functional scan were discarded to account
274 for magnetic saturation effects. Structural scans were processed using Freesurfer^{24,25} to generate
275 a 3D model of the cortex. We created flat patches of unfolded cortex for each hemisphere (120
276 mm in diameter), centred on the occipital pole (see Figure 3) to facilitate data visualisation and
277 the creation of Regions of Interest (ROIs). The ring and wedge retinotopy and localiser scans
278 were summarised by a coherence (travelling wave) analysis²⁶ to calculate the phase of the BOLD
279 response at the repetition frequency of the stimulus for each voxel. The pRF data were fit by
280 estimating (at each voxel) the parameters of a 2D Gaussian function that best predicted the BOLD
281 timecourse, given the position of the bar stimulus²⁷. This was done independently for the left and
282 right eye scans. The contrast response function data were combined across repetition and
283 analysed using a general linear model (GLM), with regressors (β weights) for each of the 25
284 conditions. We used a combination of retinotopy and pRF results to define a V1 ROI on the
285 flattened cortex using the location of the calcarine sulcus and reversals of phase angle. ROIs
286 were further restricted using the localiser data, by retaining voxels with a coherence exceeding
287 0.3. Results were saved as Matlab files, and imported into *R* for statistical analysis and
288 visualisation. We also converted GLM β weights to MNI space (using tools from FSL²⁸), and
289 averaged them across participants for visualisation on an inflated cortex in the Connectome
290 Workbench software²⁹.

291

292 *EEG acquisition*

293

294 All EEG data were acquired using a 64-channel ANT Neuroscan system, with electrodes
295 positioned in a Waveguard cap according to the 10-20 system. Signals were recorded at 1000Hz,
296 and referenced to the whole-head average. Low-latency digital triggers were sent from the
297 stimulus computer to the EEG amplifier using a parallel cable, and recorded stimulus onset and
298 condition codes to the EEG trace. Participants completed 8 repetitions of the contrast response
299 function experiment. On each repetition, stimuli were presented for trials of 12 seconds, with an
300 intertrial interval of 3 seconds. All 25 conditions (see Figure 2g) were presented once per
301 repetition in a random order, taking 375 seconds per block. Participants were given breaks

302 between blocks. The same fixation task as described for the MRI experiments was performed
303 throughout the experiment to maintain attention.

304

305 *EEG analysis*

306

307 Raw data were converted to a compressed csv format using functions from EEGlab³⁰, and were
308 then imported into R for analysis. We took the Fourier transform of the EEG waveform at each
309 electrode, for a ten-second window beginning one second after stimulus onset (to avoid onset
310 transients). Fourier spectra were averaged across four occipital electrodes (*Oz*, *POz*, *O1* and *O2*),
311 and across repetition, using coherent averaging (i.e. retaining the phase information). We then
312 calculated signal-to-noise ratios (SNRs) by dividing the absolute amplitude in the signal bin (4Hz)
313 by the mean of the ten adjacent bins (± 0.5 Hz in steps of 0.1Hz). These SNRs were averaged
314 across participants, and standard errors were calculated using bootstrapping. To plot the
315 timecourse of SSVEP activity, we repeated the Fourier transform using a sliding one-second
316 window (in steps of 10ms), and scaled by the two adjacent bins (± 1 Hz) to calculate the SNR.

317

318 *Data and script availability*

319

320 Data, experiment code (in Matlab) and analysis code (in Matlab and R) is available at:
321 <http://dx.doi.org/10.17605/OSF.IO/X9ZR8>

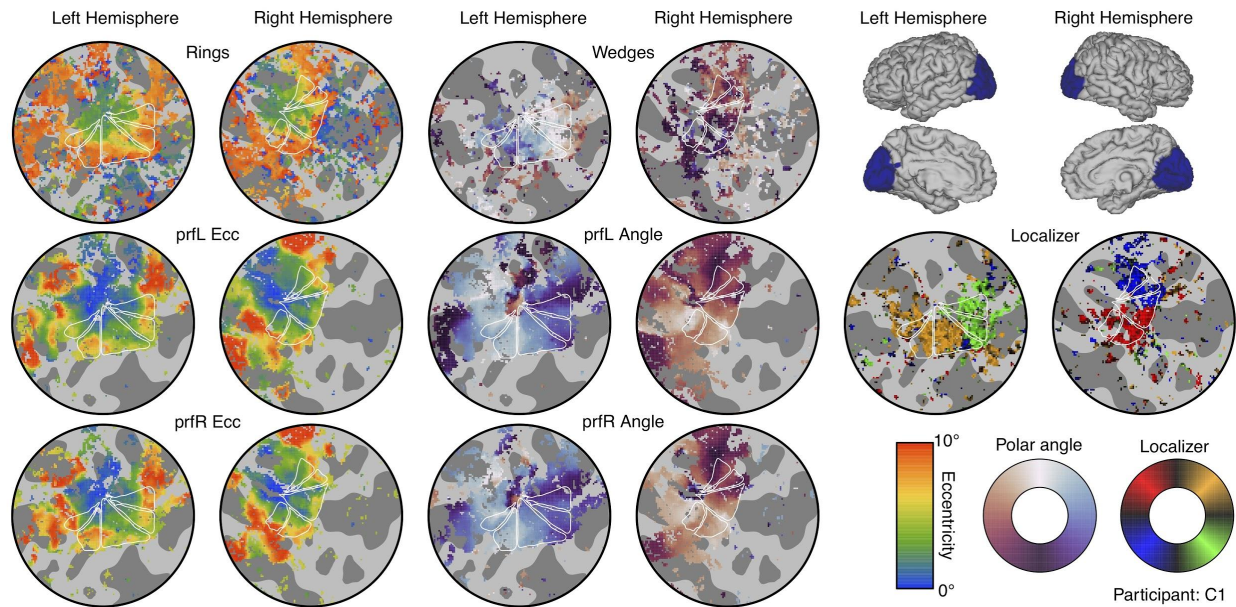
322

323 **Results**

324

325 We used the results from retinotopic mapping scans with ring and wedge stimuli (Figure 2a,b),
326 and population receptive field (pRF) sequences (Figure 2c,e), to identify primary visual cortex
327 (V1) on flattened discs of occipital cortex for each hemisphere. Example flat maps are shown in
328 Figure 3 for one control participant (see the project repository for equivalent plots for all
329 participants: <https://osf.io/x9zr8/>). The phase angle of the BOLD response to the ring stimuli, and
330 the pRF eccentricity values, showed a typical central-to-peripheral gradient²⁷, and were highly
331 consistent (e.g. across left and right eye pRF sequences). The phase angle across the wedge
332 and pRF scans showed strong hemisphere/hemi-field segregation (i.e. the right hemisphere
333 responded to stimuli in the left hemi-field and vice versa), as well as the expected phase
334 reversals³¹ that were used to determine boundaries between V1, V2 and V3 (shown by the white
335 triangles in each map - the middle triangle is V1). The V1 region-of-interest (ROI) was further
336 restricted using the responses to a phase-encoded localiser stimulus (see Figure 2d). These
337 responses also showed strong hemisphere/hemi-field and dorsal/ventral segregation, and we
338 retained voxels in the V1 ROI that produced responses with a coherence of 0.3 or higher (right-
339 most flat maps in Figure 3). This resulted in a mean total V1 ROI size (combined across
340 hemispheres) of 601 voxels, and no significant difference in ROI size between patients and
341 controls ($t(20)=0.54$, $p=0.60$).

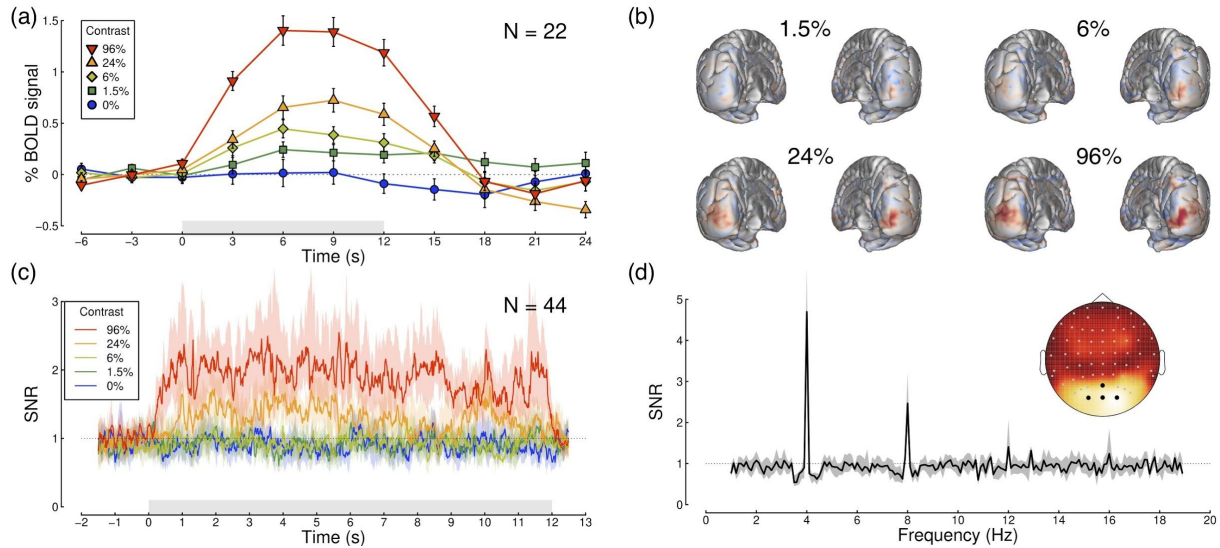
342



343
344 Figure 3: Summary of retinotopic mapping and functional localizer results. The icons in the upper right
345 corner indicate the region of cortex in each hemisphere used to make the flat maps (each 120 mm in
346 diameter). The left-most columns show eccentricity estimates from a plaid ring localiser (top row), and pRF
347 models for stimuli shown to the left (middle row) and right (lower row) eyes. The middle columns show the
348 polar angle parameter from a rotating plaid wedge localiser (top row) and the two pRF models (middle and
349 lower rows). The flat maps in the right-most columns show the responses to the phase-encoded plaid
350 localiser. Colour maps for each measure are shown in the lower right corner. In each flat map, dark grey
351 regions indicate sulci, and white triangles show the locations of visual areas V1 (middle triangle) and
352 V2/3v/d (outer triangles). The phase encoded retinotopy and localiser results were thresholded at a
353 coherence value of 0.3, and the pRF results were thresholded at 10% of explained variance.

354
355 The localiser-restricted V1 ROIs for each participant were then used to estimate neural responses
356 to stimuli of different contrasts presented to the two eyes (Figure 2f). The BOLD response in this
357 ROI had a typical timecourse³², which was modulated by stimulus contrast (see Figure 4a). We
358 fitted a general linear model (GLM) to the full timecourse to estimate a β coefficient for each
359 stimulus condition at each voxel. The β weights were strongly modulated by stimulus contrast at
360 the occipital pole (red shading in Figure 4b). In a separate experiment using identical stimuli, we
361 also recorded steady-state visual evoked potentials (SSVEPs) using EEG. These showed clear
362 modulation of signal-to-noise ratio (SNR) with stimulus contrast at the flicker frequency of the
363 stimuli (4Hz, Figure 2g), but with a less sluggish timecourse than the BOLD response (see Figure
364 4c). The responses were well-isolated in the Fourier amplitude spectrum (see Figure 4d), and
365 localised to occipital electrodes (Figure 4d inset). We therefore used the fMRI β weights averaged
366 across the ROI, and the SSVEP SNRs averaged across four occipital electrodes (black points in
367 the Figure 4d inset) to calculate contrast response functions for each experiment. Exploratory
368 analyses in V2 and V3, and using different localiser thresholds to define the V1 ROI, produced
369 very similar functions (not shown), as did using raw amplitude values for the EEG experiment
370 (rather than SNR values).

371



372
373
374
375
376
377
378
379
380
381
382
383
384
385
386
387
388
389
390
391
392
393
394
395
396
397
398
399
400
401
402

Figure 4: Timecourses and topographies of visual responses measured using fMRI and EEG. Panel (a) shows the BOLD timecourse in the localiser-restricted V1 ROI, for binocular presentation at five stimulus contrasts (see legend). The grey rectangle adjacent to the x-axis indicates the period when the stimulus was presented, and error bars indicate ± 1 SE across participants (N=22). Panel (b) shows averaged beta weights (unthresholded) from the general linear model, projected on a posterior view of each hemisphere, for the non-zero stimulus contrasts averaged across all participants (subtracting the 0% condition as a baseline). Panel (c) shows the SSVEP timecourse as a signal-to-noise ratio (SNR) at the target flicker frequency (4Hz), calculated using a 1000ms sliding window (centred at the time indicated on the x-axis). Shaded regions indicate bootstrapped 95% confidence intervals of the median, calculated across participants (N=44). The grey shaded rectangle represents the period when the stimulus was presented. Panel (d) shows the Fourier spectrum for a 96% contrast binocular target, averaged across all participants (N=44), for 10-second windows of stimulation. Clear peaks in SNR are apparent at the stimulus flicker frequency (4Hz) and its harmonics (especially 8Hz). The grey shaded region indicates 95% confidence intervals of the median. The inset scalp topography shows that responses were strongest at posterior electrode sites over early visual areas. For panels (c,d), signals were averaged across the electrodes indicated in black on the scalp plot (Oz, POz, O1 and O2).

Figure 5 shows contrast response functions from both experiments, split by participant group (control participants in Figure 5a,c, patients in Figure 5b,d). The first contrast response function in each row (circle symbols) is for monocular stimulus presentation, and shows the expected monotonic increase for each data set. As predicted by our computational models (see Figure 1), as mask contrast increased, the functions rose from baseline across the plot. Statistically, there were significant main effects of both target and mask contrast, and significant interactions, for all data sets (see Table 2). For the patients there was a very slight reduction of response in the amblyopic eye (orange circles) compared with the fellow eye (blue circles) at the highest target contrast in the fMRI data (Figure 5b), though this was not significant ($t(11)=1.20$, $p=0.26$, $d=0.35$). The difference was more pronounced in the SSVEP data (Figure 5d), and was significant at 24% target contrast ($t(24)=2.91$, $p<0.01$, $d=0.58$), though not at 96% contrast ($t(24)=1.96$, $p=0.06$, $d=0.39$).

403 For the control participants, there was evidence of interocular suppression (a u-shaped function)
 404 for the highest mask contrast when measured using fMRI (final function in Figure 5a), though this
 405 was not statistically significant (paired samples t-test comparing 0% and 6% target contrast
 406 conditions when a 96% contrast mask was present, $t(9)=1.8$ $p=0.10$, $d=0.57$, mean difference of
 407 0.13 β units). For the control EEG data interocular suppression occurred at a higher target
 408 contrast (96%, see final function in Figure 5c), but was also not significant ($t(18)=0.96$, $p=0.35$,
 409 $d=0.22$, mean difference of 0.44 SNR units). The u-shaped function was more pronounced in the
 410 patients (Figure 5b,d). For the fMRI data, suppression was more substantial when the mask was
 411 shown to the fellow eye (orange inverted triangles comparing 0% and 6% target levels with a 96%
 412 mask; $t(11)=3.25$, $p=0.008$, $d=0.94$, mean difference of 0.46 β units) than the amblyopic eye (blue
 413 inverted triangles; $t(11)=2.51$, $p=0.029$, $d=0.72$, mean difference of 0.22 β units). A very subtle
 414 suppression effect was qualitatively apparent for the SSVEP data (Figure 5d), but this did not
 415 reach statistical significance for either eye (both $p>0.05$). SSVEP responses at the second
 416 harmonic frequency (8Hz) were broadly similar to those at the fundamental (see Supplementary
 417 Figure S1).

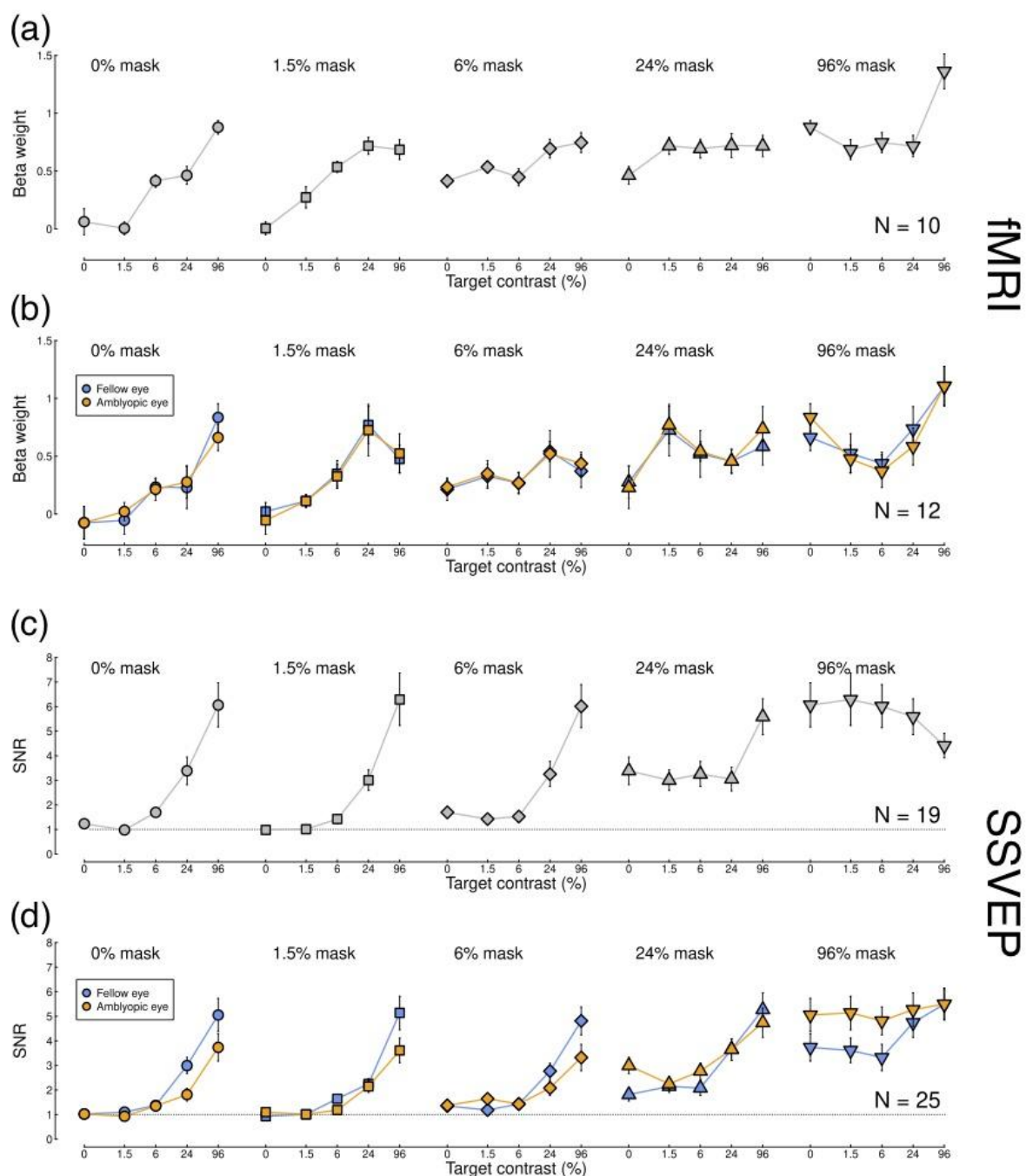
418

419 Table 2: ANOVA results for contrast response functions.

Data set	Effect	F-ratio (df)	p-value	Effect size (ω^2)
Control fMRI	Left eye contrast	18.82 (4,36)	<0.001	0.27
Control fMRI	Right eye contrast	19.56 (4,36)	<0.001	0.22
Control fMRI	Interaction	2.91 (16,144)	<0.001	0.18
Patient fMRI	Fellow eye contrast	12.80 (4,44)	<0.001	0.14
Patient fMRI	Amblyopic eye contrast	8.47 (4,44)	<0.001	0.14
Patient fMRI	Interaction	2.92 (16,176)	<0.001	0.15
Control SSVEP	Left eye contrast	29.93 (4,72)	<0.001	0.31
Control SSVEP	Right eye contrast	27.21 (4,72)	<0.001	0.28
Control SSVEP	Interaction	6.43 (16,288)	<0.001	0.14
Patient SSVEP	Fellow eye contrast	34.88 (4,96)	<0.001	0.38
Patient SSVEP	Amblyopic eye contrast	19.26 (4,96)	<0.001	0.17
Patient SSVEP	Interaction	2.96 (16,384)	<0.001	0.04

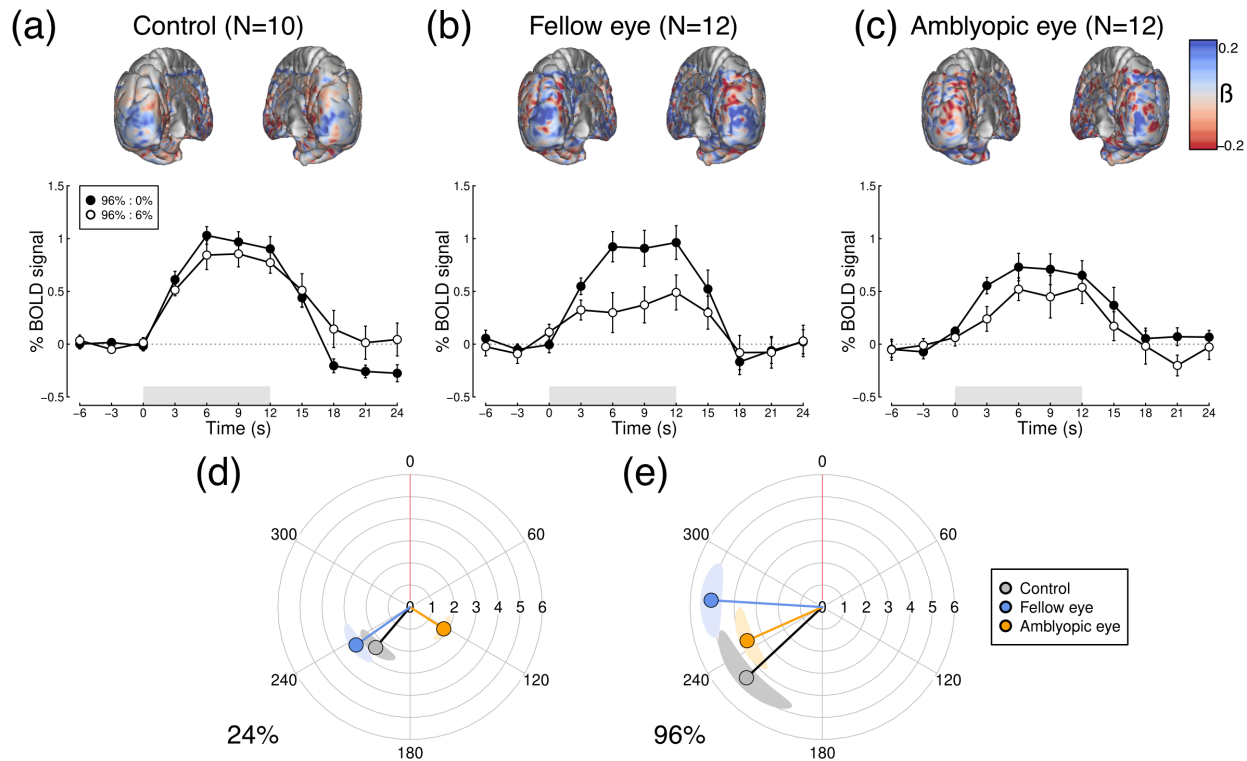
420

421



422
 423 Figure 5: Contrast response functions measured using fMRI and EEG. Data for control participants (panels
 424 a,c) are averaged across complementary conditions for the left and right eyes. Data for patients (panels
 425 b,d) are plotted considering the fellow eye as the 'target' eye (blue) and also considering the amblyopic eye
 426 as the 'target' eye (orange). These data are identical, but are re-ordered to aid interpretation. Error bars in
 427 each plot indicate $\pm 1SE$ across participants.
 428

429 To further investigate the interocular suppression effect, we plotted full BOLD timecourses for the
430 condition where the mask only was shown (96% contrast mask to one eye, 0% contrast target to
431 the other), and the condition where the same mask was paired with a 6% contrast target in the
432 other eye (see Figure 6). Interocular suppression is clear in each data set, as the white points
433 appear below the black points over much of the function. Our computational model (see right-
434 most functions in Figure 1a,c) predicts that this happens because the excitatory impact of the 6%
435 contrast stimulus is outweighed by its suppression of the response to the 96% contrast stimulus
436 in the other eye: overall activity goes down instead of up. However this effect is much more
437 substantial for the fellow eye of the patients (Figure 6b) than for the amblyopic eye (Figure 6c),
438 consistent with our finding from the β weights (Figure 5b). The cortical meshes along the upper
439 row of Figure 6 show the difference in β weights between conditions, with blue shading indicating
440 stronger suppression. Suppression is apparent at the occipital pole, and is again strongest for the
441 fellow eye of the patients (Figure 6b).
442



443
444 Figure 6: Timecourse and spatial distribution of interocular suppression measured using fMRI, and polar
445 plots of SSVEP responses to monocular stimuli. Upper plots show the difference of β weights at each voxel
446 (unthresholded), between a monocular condition where one eye saw 96% contrast, and a dichoptic
447 condition where the eyes saw 96% and 6% contrast. Blue shading indicates a suppressive effect (and red
448 shading a facilitatory effect) of the 6% component. Lower panels show the timecourse of % signal change
449 for the same two conditions. Data are shown for (a) control participants, (b) the 96% contrast mask in the
450 fellow eye of the patients, and (c) the 96% contrast mask in the amblyopic eye of the patients. Error bars
451 indicate ± 1 SE across participants, and grey shaded rectangles show the duration of stimulus presentation.
452 Panels (d,e) show SSVEP responses for monocularly presented stimuli at 24% (d) and 96% (e)
453 contrast. This representation shows a phase lag (i.e. angular difference) between the amblyopic (orange)
454 and fellow (blue) eyes. Shaded regions indicate ± 1 SE, calculated independently for amplitude and phase values.

455 The lower two panels of Figure 6 show polar plots comparing monocular SSVEP responses to
456 stimuli of 24% contrast (Fig 6d), and 96% contrast (Fig 6e). There is a phase lag between the
457 fellow and amblyopic eye in both panels. For the 24% contrast target, this is approximately 112
458 degrees, which corresponds to a lag of around 78 ms at the 4Hz flicker frequency used here. For
459 the 96% contrast, the lag is around 28 degrees (20 ms). This latter estimate corresponds well with
460 previously reported phase lags using a similar paradigm in magnetoencephalography (MEG)³³.

461

462 Discussion

463

464 We measured neural responses to different combinations of contrast in the left and right eyes,
465 using both EEG and fMRI. In participants with atypical binocular vision, we found reduced
466 responses in the amblyopic eye using EEG, and increased suppression between the eyes
467 (compared with controls) in V1 using fMRI. These different effects are consistent with greater
468 tonic and dynamic suppression (respectively) in individuals with impaired binocular vision, and
469 may be responsible for the deficits in stereopsis experienced by the majority of these participants
470 (see Table 1). We now discuss why the results differ across measurement methods, what these
471 findings tell us about amblyopic suppression, and how treatments might be targeted towards the
472 development of functioning binocular vision.

473

474 *Comparison of EEG and fMRI measures*

475

476 This is the first study to use both EEG and fMRI to investigate contrast processing in impaired
477 binocular vision. Previous studies using either EEG or MEG^{14,33} have typically found larger
478 amblyopic deficits in the monocular response than those using fMRI^{34,35} (though some work has
479 shown substantial fMRI deficits³⁶), mirroring our results here (left-most functions of Figure 5b,d).
480 Considering only this previous work, heterogeneity of stimuli and participants across studies might
481 well have explained the differences. However in the present experiments we used identical
482 stimuli, and the same participants completed both experiments (Supplementary Figure S2 shows
483 the EEG data for only the participants who completed the MRI experiments). The reduction in
484 response amplitude to stimuli in the weaker eye is clearer using SSVEP than using fMRI.
485 However, differences in dynamic interocular suppression are only apparent when measured with
486 fMRI (right-most functions in Figure 5a,b; Figure 6a-c).

487

488 Analogous differences between these two methods have recently been reported in the study of
489 attention. Itthipuripat et al.³⁷ found that spatial attention produces a change in baseline response
490 when measured using fMRI, but not when measured using EEG (including evoked potentials and
491 SSVEPs). Instead fMRI, which measures global neural activity indirectly via oxygen consumption,
492 appears to be more closely related to late ERP components and alpha band oscillations recorded
493 using EEG³⁷, rather than the stimulus onset transients detected by SSVEP and early ERP
494 components. Although our contrast response functions do not involve baseline shifts, the other
495 differences between our fMRI and EEG results are consistent with different features of neural
496 activity being probed by these two methods.

497

498 One possible explanation for the differences in monocular response between methods is that the
499 firing of visual neurons responsive to the amblyopic eye might be desynchronised. This would
500 have a greater effect on phase-locked SSVEP responses – which depend upon synchronised
501 firing – than on fMRI BOLD responses, which are a proxy for overall neural activity. Instead,
502 asynchronous activity in higher frequency bands (50 – 200Hz) shows a closer correspondence
503 with the BOLD response³⁸, and these signals can be detected with extracranial techniques such
504 as MEG³⁹. In terms of the differences in suppression, this could reflect processing in different
505 layers of cortex. Evoked responses measured using EEG correspond most closely to activity in
506 the more superficial (supragranular) layers of cortex, whereas much inhibitory processing involves
507 deeper (granular) layers⁴⁰. Future work using laminar fMRI at higher field strength (7T or above⁴¹),
508 or multi-unit electrophysiology^{42,43}, could allow dissociation of excitatory and inhibitory responses
509 in amblyopia. In addition, these methods can resolve ocular dominance columns in V1, allowing
510 eye-specific inputs to be measured directly.

511

512 *What is amblyopic suppression?*

513

514 Suppression in amblyopia is measured very differently in clinical practice compared with the
515 methods used in lab-based neuroscience research. The most common clinical measures are the
516 Worth 4-dot test, and Bagolini striated lenses, both of which give a qualitative indication of whether
517 one eye's image is substantively suppressed by the other eye during binocular viewing. Lab-
518 based measures involve a variety of paradigms, including psychophysical approaches such as
519 dichoptic masking^{10,44–46}, or assessing binocular fusion of edges⁴⁷ or gratings⁴⁸, and more direct
520 neurophysiological estimates of suppression in animal models^{49,50}. However, because both eyes
521 are being stimulated during testing, clinical suppression could in principle be explained by either
522 tonic or dynamic suppression, and most psychophysical work also cannot distinguish between
523 these possibilities. Many of our patients (around half) no longer met the clinical criterion for
524 amblyopia, yet as a group they still exhibited greater dynamic interocular suppression than our
525 control participants, as well as tonic suppression of one eye. The finding that both types of
526 suppression are apparent, even in individuals who have received patching or surgical
527 interventions, strongly suggests that both will also be present in untreated amblyopes. Amblyopic
528 suppression might therefore involve a combination of these two processes.

529

530 One feature that remains to be determined is whether one type of suppression is a primary cause
531 of amblyopia, and the other a later consequence. Cortical suppression, characterised as a
532 process of gain control⁵¹, is a dynamic, adaptive process that acts to optimise the sensory
533 response⁵². It is clear that binocular vision is particularly plastic, as the relative weighting of the
534 two eyes can be altered following a brief period of occlusion⁵³, and this may be the mechanism
535 by which clinical patching treatment improves vision. Our finding of increased suppression of the
536 fellow eye by the amblyopic eye could be an attempt to rebalance an asymmetrical system. If so,
537 this might influence the development of novel treatments geared towards modulating interocular
538 suppression.

539

540 *Perceptual consequences of suppression, and potential for targeted treatment*

541

542 It is generally assumed that clinical suppression results in viewing the world ‘through’ the fellow
543 eye, with signals from the amblyopic eye being completely suppressed. However, other work has
544 shown that when signals in the amblyopic eye are boosted by an appropriate amount, information
545 is still summed binocularly⁵⁴. Indeed, the principle of ocularity invariance (that the world does not
546 change when one eye is closed) makes it very difficult to distinguish between suppression and
547 fusion outside of the laboratory or clinic. However, even if the amblyopic eye still contributes to
548 perception, stereopsis is extremely sensitive to imbalances between the eyes, and breaks down
549 when one eye receives a stronger input⁵⁵. The two types of suppression we identify here would
550 likely unbalance signals in exactly this way, which may contribute to the poorer stereopsis for
551 most of our patients (see Table 1).

552
553 Consistent with this idea, several treatments have recently been proposed that aim to reduce
554 suppression between the eyes. For example, antisuppression therapy⁵⁶ involves presenting dot
555 motion stimuli, in which signals are shown to one eye, and noise distractors to the other. To
556 perform the task, patients must favour information from the signal (amblyopic) eye. Performance
557 improves over time, implying that suppression is reduced. This approach also improves acuity
558 and stereopsis, even in amblyopic adults far beyond the critical period (in childhood) for traditional
559 treatment. Related treatments that involve playing dichoptic video games⁵⁷⁻⁵⁹, or watching
560 dichoptic movies⁶⁰, may work in a similar way. Measuring the two types of suppression identified
561 here throughout treatment would reveal causal relationships between suppression and visual
562 function, potentially allowing clinicians to optimise treatment schedules and monitor progress.

563

564 **Appendix 1 – details of computational models**

565
566 The two stage model of Meese et al.¹⁶ comprises an initial stage of monocular gain control,
567 followed by binocular summation, defined as:

568

$$569 \quad \text{binsum} = \frac{C_L^m}{S + C_L + \omega_R C_R} + \frac{C_R^m}{S + C_R + \omega_L C_L}$$

570
571 where $m = 1.3$, $S = 1$, and $\omega_R = \omega_L = 1$, C_L and C_R are the input contrasts to the left and right eyes.

572 The output of the model follows a further nonlinearity:

573

$$574 \quad \text{resp} = \frac{\text{binsum}^p}{Z + \text{binsum}^q}$$

575
576 where $p = 8$, $q = 6.5$, and $Z = 0.1$. The predictions shown in Figure 1a are the output of the model

577 for different combinations of C_L and C_R . To predict the effects of attenuating one eye’s input

578 (Figure 1b), an attenuator parameter¹⁰ is added to one eye’s input:

579

$$580 \quad \text{binsum} = \frac{aC_L^m}{S + aC_L + \omega_R C_R} + \frac{C_R^m}{S + C_R + \omega_L aC_L}$$

581

582 where $a = 0.5$. Finally, to assess the impact of unbalanced interocular suppression (Figure 1c),
583 we set $\omega_R = 2$, but left $\omega_L = 1$ (and set $a = 1$). Precise parameter values, e.g. of exponents, are
584 not essential to produce the overall model behaviour.

585

586 Acknowledgements

587

588 We are grateful to all of our participants for their involvement in this work, and to Robert Hess for
589 helpful discussions on suppression in amblyopia.

590

591 References

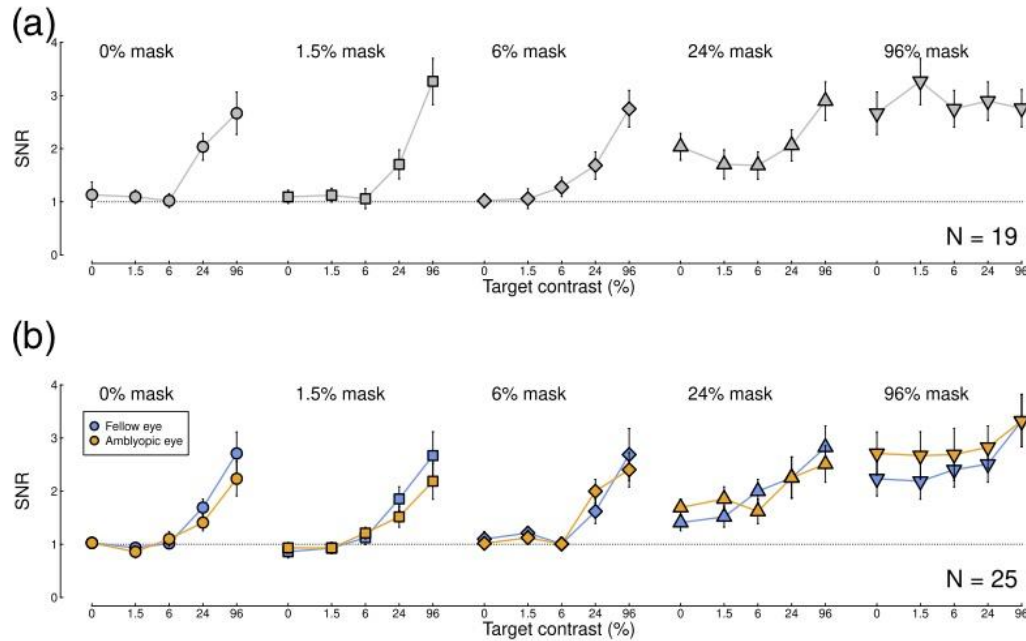
592

- 593 1. Coutant BE, Westheimer G. Population distribution of stereoscopic ability. *Ophthalmic and*
594 *Physiological Optics* 1993;13:3–7.
- 595 2. Julesz B. Stereoscopic vision. *Vision Res* 1986;26:1601–1612.
- 596 3. Fu Z, Hong H, Su Z, et al. Global prevalence of amblyopia and disease burden projections through
597 2040: a systematic review and meta-analysis. *British Journal of Ophthalmology* 2020;104:1164–1170.
- 598 4. Hess RF. Contrast sensitivity assessment of functional amblyopia in humans. *Trans Ophthalmol Soc U*
599 *K* 1979;99:391–397.
- 600 5. Levi DM. Rethinking amblyopia 2020. *Vision Research* 2020;176:118–129.
- 601 6. Levi DM, Knill DC, Bavelier D. Stereopsis and amblyopia: A mini-review. *Vision Research*
602 2015;114:17–30.
- 603 7. Jampolsky A. Characteristics of Suppression in Strabismus. *Archives of Ophthalmology* 1955;54:683–
604 696.
- 605 8. Pratt-Johnson JA, Tillson G. Suppression in strabismus--an update. *British Journal of Ophthalmology*
606 1984;68:174–178.
- 607 9. Travers T aB. Suppression of vision in squint and its association with retinal correspondence and
608 amblyopia. *British Journal of Ophthalmology* 1938;22:577–604.
- 609 10. Baker DH, Meese TS, Hess RF. Contrast masking in strabismic amblyopia: attenuation, noise,
610 interocular suppression and binocular summation. *Vision Res* 2008;48:1625–1640.
- 611 11. Baker DH, Meese TS, Georgeson MA. Binocular interaction: contrast matching and contrast
612 discrimination are predicted by the same model. *Spatial Vision* 2007;20:397–413.
- 613 12. Levelt WJM. The alternation process in binocular rivalry. *British Journal of Psychology* 1966;57:225–
614 238.
- 615 13. Ding J, Levi DM. Rebalancing binocular vision in amblyopia. *Ophthalmic and Physiological Optics*
616 2014;34:199–213.
- 617 14. Baker DH, Simard M, Saint-Amour D, Hess RF. Steady-State Contrast Response Functions Provide
618 a Sensitive and Objective Index of Amblyopic Deficits. *Investigative Ophthalmology & Visual Science*
619 2015;56:1208–1216.
- 620 15. Barnes GR, Hess RF, Dumoulin SO, et al. The cortical deficit in humans with strabismic amblyopia.
621 *The Journal of Physiology* 2001;533:281–297.
- 622 16. Meese TS, Georgeson MA, Baker DH. Binocular contrast vision at and above threshold. *J Vis*
623 2006;6:1224–1243.
- 624 17. Moradi F, Heeger DJ. Inter-ocular contrast normalization in human visual cortex. *J Vis* 2009;9:13.1-
625 22.
- 626 18. Baker DH, Wade AR. Evidence for an Optimal Algorithm Underlying Signal Combination in Human
627 Visual Cortex. *Cerebral Cortex* 2017;27:254–264.
- 628 19. Baker DH, Meese TS, Georgeson MA. Paradoxical Psychometric Functions (“Swan Functions”) are
629 Explained by Dilution Masking in Four Stimulus Dimensions. *i-Perception* 2013;4:17–35.
- 630 20. Baker DH, Kaestner M, Gouws AD. Measurement of crosstalk in stereoscopic display systems used
631 for vision research. *Journal of Vision* 2016;16:14.
- 632 21. Brainard DH. The Psychophysics Toolbox. *Spat Vis* 1997;10:433–436.
- 633 22. Kleiner M, Brainard DH, Pelli DG. What’s new in Psychtoolbox-3? *Perception* 2007;36(S):14.

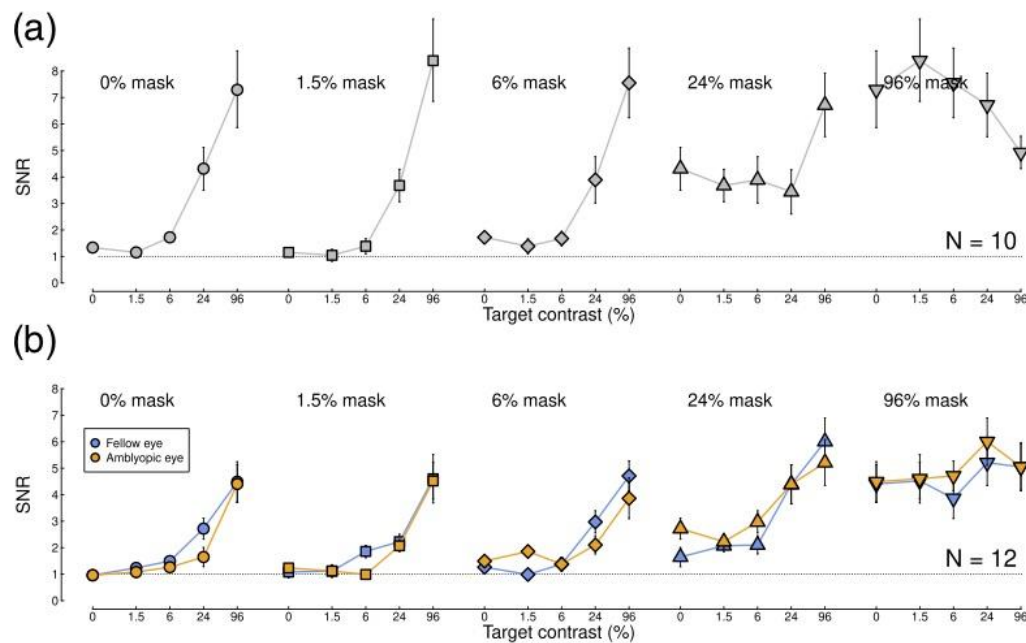
- 634 23. Pelli DG. The VideoToolbox software for visual psychophysics: transforming numbers into movies.
635 *Spat Vis* 1997;10:437–442.
- 636 24. Dale AM, Fischl B, Sereno MI. Cortical surface-based analysis. I. Segmentation and surface
637 reconstruction. *Neuroimage* 1999;9:179–194.
- 638 25. Fischl B. FreeSurfer. *Neuroimage* 2012;62:774–781.
- 639 26. Engel SA, Rumelhart DE, Wandell BA, et al. fMRI of human visual cortex. *Nature* 1994;369:525.
- 640 27. Dumoulin SO, Wandell BA. Population receptive field estimates in human visual cortex. *NeuroImage*
641 2008;39:647–660.
- 642 28. Jenkinson M, Beckmann CF, Behrens TEJ, et al. FSL. *Neuroimage* 2012;62:782–790.
- 643 29. Marcus DS, Harwell J, Olsen T, et al. Informatics and data mining tools and strategies for the human
644 connectome project. *Front Neuroinform* 2011;5:4.
- 645 30. Delorme A, Makeig S. EEGLAB: an open source toolbox for analysis of single-trial EEG dynamics
646 including independent component analysis. *J Neurosci Methods* 2004;134:9–21.
- 647 31. Sereno MI, Dale AM, Reppas JB, et al. Borders of Multiple Visual Areas in Humans Revealed by
648 Functional Magnetic Resonance Imaging. *Science* 1995;268:889–893.
- 649 32. Boynton GM, Engel SA, Glover GH, Heeger DJ. Linear systems analysis of functional magnetic
650 resonance imaging in human V1. *J Neurosci* 1996;16:4207–4221.
- 651 33. Chadnova E, Reynaud A, Clavagnier S, Hess RF. Latent binocular function in amblyopia. *Vision*
652 *Research* 2017;140:73–80.
- 653 34. Conner IP, Odom JV, Schwartz TL, Mendola JD. Monocular activation of V1 and V2 in amblyopic
654 adults measured with functional magnetic resonance imaging. *J AAPOS* 2007;11:341–350.
- 655 35. Li X, Dumoulin SO, Mansouri B, Hess RF. Cortical Deficits in Human Amblyopia: Their Regional
656 Distribution and Their Relationship to the Contrast Detection Deficit. *Investigative Ophthalmology &*
657 *Visual Science* 2007;48:1575.
- 658 36. Hess RF, Li X, Lu G, et al. The contrast dependence of the cortical fMRI deficit in amblyopia; a
659 selective loss at higher contrasts. *Human Brain Mapping* 2010;31:1233–1248.
- 660 37. Itthipuripat S, Sprague TC, Serences JT. Functional MRI and EEG Index Complementary Attentional
661 Modulations. *The Journal of Neuroscience* 2019;39:6162–6179.
- 662 38. Hermes D, Nguyen M, Winawer J. Neuronal synchrony and the relation between the blood-oxygen-
663 level dependent response and the local field potential. *PLOS Biology* 2017;15:e2001461.
- 664 39. Kupers ER, Wang HX, Amano K, et al. A non-invasive, quantitative study of broadband spectral
665 responses in human visual cortex. *PLOS ONE* 2018;13:e0193107.
- 666 40. Bruyns-Haylett M, Luo J, Kennerley AJ, et al. The neurogenesis of P1 and N1: A concurrent
667 EEG/LFP study. *NeuroImage* 2017;146:575–588.
- 668 41. de Hollander G, van der Zwaag W, Qian C, et al. Ultra-high resolution fMRI reveals origins of
669 feedforward and feedback activity within laminae of human ocular dominance columns. *BioRxiv*
670 preprint; 2020. Available at: <http://biorxiv.org/lookup/doi/10.1101/2020.05.19.102186>.
- 671 42. Hirsch JA, Martinez LM, Pillai C, et al. Functionally distinct inhibitory neurons at the first stage of
672 visual cortical processing. *Nature Neuroscience* 2003;6:1300–1308.
- 673 43. Martinez LM, Wang Q, Reid RC, et al. Receptive field structure varies with layer in the primary visual
674 cortex. *Nature Neuroscience* 2005;8:372–379.
- 675 44. Harrad RA, Hess RF. Binocular integration of contrast information in amblyopia. *Vision Res*
676 1992;32:2135–2150.
- 677 45. Huang P-C, Baker DH, Hess RF. Interocular suppression in normal and amblyopic vision: Spatio-
678 temporal properties. *Journal of Vision* 2012;12:29–29.
- 679 46. Zhou J, Reynaud A, Yao Z, et al. Amblyopic Suppression: Passive Attenuation, Enhanced Dichoptic
680 Masking by the Fellow Eye or Reduced Dichoptic Masking by the Amblyopic Eye? *Investigative*
681 *Ophthalmology & Visual Science* 2018;59:4190.
- 682 47. Spiegel DP, Baldwin AS, Hess RF. The Relationship Between Fusion, Suppression, and Diplopia in
683 Normal and Amblyopic Vision. *Investigative Ophthalmology & Visual Science* 2016;57:5810.
- 684 48. Ding J, Klein SA, Levi DM. Binocular combination in abnormal binocular vision. *Journal of Vision*
685 2013;13:14.
- 686 49. Sengpiel F, Blakemore C. Interocular control of neuronal responsiveness in cat visual cortex. *Nature*
687 1994;368:847–850.
- 688 50. Shooner C, Hallum LE, Kumbhani RD, et al. Asymmetric Dichoptic Masking in Visual Cortex of
689 Amblyopic Macaque Monkeys. *The Journal of Neuroscience* 2017;37:8734–8741.

- 690 51. Carandini M, Heeger DJ. Normalization as a canonical neural computation. *Nat Rev Neurosci*
691 2012;13:51–62.
- 692 52. Westrick ZM, Heeger DJ, Landy MS. Pattern Adaptation and Normalization Reweighting. *J Neurosci*
693 2016;36:9805–9816.
- 694 53. Lunghi C, Burr DC, Morrone C. Brief periods of monocular deprivation disrupt ocular balance in
695 human adult visual cortex. *Current Biology* 2011;21:R538–R539.
- 696 54. Baker DH, Meese TS, Mansouri B, Hess RF. Binocular Summation of Contrast Remains Intact in
697 Strabismic Amblyopia. *Investigative Ophthalmology & Visual Science* 2007;48:5332.
- 698 55. Legge GE, Gu YC. Stereopsis and contrast. *Vision Res* 1989;29:989–1004.
- 699 56. Hess RF, Mansouri B, Thompson B. A binocular approach to treating amblyopia: antisuppression
700 therapy. *Optom Vis Sci* 2010;87:697–704.
- 701 57. Backus BT, Dornbos BD, Tran TA, et al. Use of virtual reality to assess and treat weakness in human
702 stereoscopic vision. *Electronic Imaging* 2018;2018:109-1-109–6.
- 703 58. Li J, Thompson B, Deng D, et al. Dichoptic training enables the adult amblyopic brain to learn.
704 *Current Biology* 2013;23:R308–R309.
- 705 59. Vedamurthy I, Nahum M, Bavelier D, Levi DM. Mechanisms of recovery of visual function in adult
706 amblyopia through a tailored action video game. *Scientific Reports* 2015;5. Available at:
707 <http://www.nature.com/articles/srep08482>.
- 708 60. Bossi M, Taylor VK, Anderson EJ, et al. Binocular Therapy for Childhood Amblyopia Improves Vision
709 Without Breaking Interocular Suppression. *Invest Ophthalmol Vis Sci* 2017;58:3031–3043.
- 710

711 **Online Supplemental materials**
712



713
714 Figure S1: SSVEP data for the second harmonic (2F) response. The main trends are the same
715 as in Figure 5c,d, though the SNRs are overall lower (note y-axis scaling). Panel (a) shows data
716 from control participants (N=19), and panel (b) shows data from patients (N=25).
717



718
719 Figure S2: SSVEP data for only the participants who completed the fMRI experiment. The main
720 trends are the same as in Figure 5c,d. Panel (a) shows data from control participants (N=10), and
721 panel (b) shows data from patients (N=12).